

Macroscopic Impacts of Cloud and Precipitation Processes in Shallow Convection

Wojciech W. GRABOWSKI¹, Joanna SLAWINSKA²,
Hanna PAWLOWSKA², and Andrzej A. WYSZOGRODZKI¹

¹National Center for Atmospheric Research, Boulder, CO, USA
e-mail: grabow@ncar.ucar.edu (corresponding author)

²Institute of Geophysics, Faculty of Physics,
University of Warsaw, Warsaw, Poland

Abstract

This paper presents application of the EULAG model combined with a sophisticated double-moment warm-rain microphysics scheme to the model intercomparison case based on RICO (Rain in Cumulus over Ocean) field observations. As the simulations progress, the cloud field gradually deepens and a relatively sharp temperature and moisture inversions develop in the lower troposphere. Two contrasting aerosol environments are considered, referred to as pristine and polluted, together with two contrasting subgrid-scale mixing scenarios, the homogeneous and the extremely inhomogeneous mixing. Pristine and polluted environments feature mean cloud droplet concentrations around 40 and 150 mg^{-1} , respectively, and large differences in the rain characteristics. Various measures are used to contrast evolution of macroscopic cloud field characteristics, such as the mean cloud fraction, the mean cloud width, or the height of the center of mass of the cloud field, among others. Macroscopic characteristics appear similar regardless of the aerosol characteristics or the homogeneity of the subgrid-scale mixing.

Key words: shallow convection, cloud microphysics, CNN activation, homogeneity of subgrid-scale mixing.

1. INTRODUCTION

Due to limited computational resources, global climate models typically feature relatively low spatial and temporal resolutions, tens of kilometers and minutes at best. In such models, cloud and precipitation processes can be taken into account only through appropriate parameterizations. These parameterizations are supposed to mimic our understanding of cloud dynamics and microphysics as well as their interactions with larger-scale processes. The understanding comes from cloud observations and process studies applying smaller-scale models of various complexity (*i.e.*, mesoscale models, cloud-resolving models, large-eddy simulation models, direct numerical simulation models, *etc.*). A better understanding of cloud processes is the key to better climate model parameterizations. Numerical simulations reported in this paper contribute to this general goal.

Tropical and subtropical boundary layer clouds, such as subtropical stratocumulus and trade-wind cumulus, reflect back to space a significant fraction of the incoming solar radiation. At the same time their impact on the top-of-the-atmosphere (TOA) outgoing longwave radiation is relatively small because the cloud top temperatures are close to the temperature of the underlying surface. It follows that these clouds exert a significant cooling on the climate system, and they have been shown to play key role in the climate change and climate sensitivity (*e.g.*, Bony and Dufresne 2005). Because boundary layer clouds affect mostly solar radiation, their microphysical properties (*i.e.*, the spatial variability of cloud droplets spectra) in addition to their macroscopic features (such as the cloud fraction or the mean liquid water path) are relevant. Microphysical properties are to a large extent determined by the properties of the cloud condensation nuclei (CCN) and the cloud-base updraft strength, together with still poorly-understood microphysical transformation resulting from entrainment and mixing (including in-cloud activation; see discussion in Slawinska *et al.* 2011). Shallow convective clouds are known to be significantly diluted by entrainment (*e.g.*, Warner 1955 and numerous subsequent studies) and microphysical effects of entrainment (*i.e.*, homogeneity of cloud-environment mixing or entrainment-related activation) need to be considered. Recent modeling studies (*e.g.*, Chosson *et al.* 2004, 2007, Grabowski 2006, Slawinska *et al.* 2008) demonstrate that assumptions concerning the microphysical evolution of these clouds, the homogeneity of cloud-environment mixing in particular, significantly affect the albedo of a field of shallow convective clouds.

Cloud and precipitation processes have been argued to potentially affect macroscopic properties of shallow convective clouds in a variety of ways. Perhaps the most obvious is the impact of modified CCN on albedo of a cloud field through the effect on the the spectrum of cloud droplets. This is typically referred to as the first indirect aerosol effect or the Twomey effect (Twomey 1974,

1977). More recently, the smaller sizes of cloud droplets in polluted shallow cumuli were shown to affect the cloud dynamics through the impact of the rate of cloud droplet evaporation and thus the evaporative cooling near cloud edges (Xue and Feingold 2006). Moreover, smaller cloud droplets for polluted clouds can lead to a slower development of drizzle and rain via the collisions/coalescence (*e.g.*, Warner 1968). This can potentially affect the abundance, extent, and lifetime of some types of clouds, such as stratocumulus or shallow convective clouds (*e.g.*, Albrecht 1989, Pincus and Baker 1994). This is referred to as the second indirect aerosol effect. Rainout of cloud condensate was also argued to slow down the deepening of shallow convection layers (Stevens 2007, Stevens and Seifert 2008). Finally, presence of rain and accompanying rain-laden downdrafts can impact boundary-layer processes, such as the initiation of new clouds and the exchange between the atmosphere and the ocean through the surface wind gustiness.

Here we report on numerical simulations of a field of shallow convective clouds to investigate some of the above effects. In contrast to non-precipitating shallow convection considered in Siebesma *et al.* (2003) and subsequently used in many studies (*e.g.*, Zhao and Austin 2005a,b; Slawinska *et al.* 2011, among others) we consider precipitating case as in vanZanten *et al.* (2011). The emphasis is on the effects of cloud and precipitation processes (*i.e.*, CCN activation, entrainment, and drizzle/rain formation) on macroscopic and microphysical properties of shallow tropical convection. The paper is organized as follows. The next section presents the model used in this study. Relevant aspects of model results, focusing on the differences between clouds developing in pristine and polluted environments, are presented in Section 3. Modeling results and their relevance to recent studies of shallow convective clouds are summarized in Section 4.

2. THE MODEL

The model used in this study is the 3D anelastic semi-Lagrangian/Eulerian model EULAG documented in Smolarkiewicz and Margolin (1997; model dynamics), Grabowski and Smolarkiewicz (1996; model thermodynamics), and Margolin *et al.* (1999; subgrid-scale turbulent mixing); see Prusa *et al.* (2008) for a recent review with comprehensive list of references. The model setup follows the one used in the model intercomparison based on RICO (Rain in Cumulus over Ocean) field observations (see vanZanten *et al.* 2011) in which EULAG participated. A three-week period with relatively suppressed convective conditions was selected for the development of the intercomparison case. This implies that only time-averaged observed conditions can be used in the comparison between model results and observations (see vanZanten *et al.* 2011 for detailed discussion and the comparison with observations).

The initial temperature profile features 740-m deep well mixed boundary layer and a stably-stratified layer (featuring a constant potential temperature gradient) between the boundary layer top and the model top at 4 km. The water vapor decreases slightly across the boundary layer and then significantly in the free troposphere. The model is forced by large-scale temperature and water vapor advective tendencies, prescribed radiative cooling, surface fluxes of heat (sensible and latent) and momentum, as well as prescribed large-scale subsidence. Surface heat fluxes are derived from the assumed sea surface temperature (SST) of 299.8 K and saturated water vapor mixing ratio using prescribed bulk surface exchange coefficients. Guided by results discussed in Stevens and Seifert (2008; see Fig. 3 in particular), we decided to run the simulations with increased horizontal and vertical resolutions compared to the model intercomparison setup in vanZanten *et al.* (2011), that is, with gridlengths of 50/20 m in the horizontal/vertical direction, instead of 100/40 m used in the intercomparison. However, the number of gridpoints in the horizontal was kept unchanged, (*i.e.*, 128×128) which implies that the horizontal domain was only a quarter of that used in vanZanten *et al.* (2011). This aspect had an adverse impact on the simulations, especially in the low-aerosol pristine case in the final couple hours of the simulations. Because of that, only results up to 21 hrs are analyzed in this paper.

In contrast to the results contributed to vanZanten *et al.* (2011) intercomparison, EULAG model is used here with the double-moment warm-rain microphysics scheme of Morrison and Grabowski (2007, 2008). The scheme predicts number concentrations (per unit mass of dry air; N_c , N_r) and mixing ratios (q_c , q_r) for cloud water and rain (subscript c and r , respectively), and also the concentration of activated CCN (N_{act}). Prediction of N_{act} is required because the cloud droplet concentration and the activated-CCN concentration may differ as a result of collision/coalescence. The concentration of cloud droplets can change inside the cloud due to additional in-cloud activation of CCN (which in turn depends on the predicted supersaturation and N_{act}) and due to entrainment of environmental air. As shown in Slawinska *et al.* (2011), in-cloud activation is a significant source of cloud droplets in shallow cumuli and it allows maintaining approximately constant-in-height mean cloud droplet concentration as typically observed (*e.g.*, Gerber *et al.* 2008, Arabas *et al.* 2009). Entrainment and mixing affect the droplet concentration through direct dilution by resolved entraining eddies and parameterized subgrid-scale turbulent transport, as well as through the prescribed mixing scenario within the warm-rain microphysics scheme. The homogeneous mixing scenario implies that the required evaporation of cloud water occurs with no change of the droplet concentration (unless all cloud water has to evaporate). In contrast, the extremely inhomogeneous mixing implies that the mean droplet radius does not change during evaporation. See Section 5 in Morrison and Grabowski (2008) for a discussion and

a computational example. It has to be stressed that the homogeneity of mixing affects the parameterized subgrid-scale mixing only. The unavoidable mixing and evaporation near cloud edge due to numerical diffusion (*e.g.*, Grabowski and Smolarkiewicz 1990) proceeds as the homogeneous mixing. As documented in the appendix of Slawinska *et al.* (2011), parameterized mixing seems to contribute significantly less to the evaporation of cloud water compared to the numerical diffusion. Because of that, as argued in Slawinska *et al.* (2011), the homogeneity of mixing simulated by the microphysics scheme has a significantly smaller impact than anticipated based on previous studies by Chosson *et al.* (2004, 2007), Grabowski (2006), and Slawinska *et al.* (2008). Current results strongly support such a conjecture because simulations with contrasting mixing scenarios differ little.

As in Morrison and Grabowski (2007, 2008) and in Slawinska *et al.* (2011), we contrast results obtained assuming either the maritime aerosol characteristics (the pristine case; the total CCN concentration of 100 mg^{-1}) or the continental aerosol characteristics (the polluted case; CCN concentration of 1000 mg^{-1}). These values are used in the CCN activation scheme as described in Morrison and Grabowski (2007) with all other parameters characterizing the aerosol exactly as described there. So the four simulations are: two pristine aerosol with homogeneous and extremely inhomogeneous mixing, referred to as 100.HM and 100.EI, respectively, and two polluted, 1000.HM and 1000.EI.

3. RESULTS

Time evolutions of model results are consistent with those presented in vanZanten *et al.* (2011; see Fig. 3 in particular). We focus on the entire evolution of the cloud field as simulated by the EULAG model, and on the effects of cloud and precipitation processes in particular. In contrast, the discussion in vanZanten *et al.* (2011) focused on the differences between participating models during the final four hours of the simulations. Significantly more results from the vanZanten *et al.* (2011) intercomparison is available at <http://www.knmi.nl/samenw/rico/LESoutputsets.html>.

3.1 The temperature and moisture profiles

Figure 1 shows instantaneous potential temperature and water vapor profiles for hours 3, 6, ..., 21 for the simulation 1000.HM. The profiles for other simulations are similar and are not shown. The initial profiles are uniform above the well-mixed boundary layer. As the simulation progresses, the initial profiles slowly evolve into profiles that are less stable and slightly more humid within the cloud layer, and are capped by a couple-hundred-meter deep inversion. The inversion slowly rises and the cloud layer gradually deepens, with the tallest clouds reaching a few hundred meters above the inversion (this will become evident in the

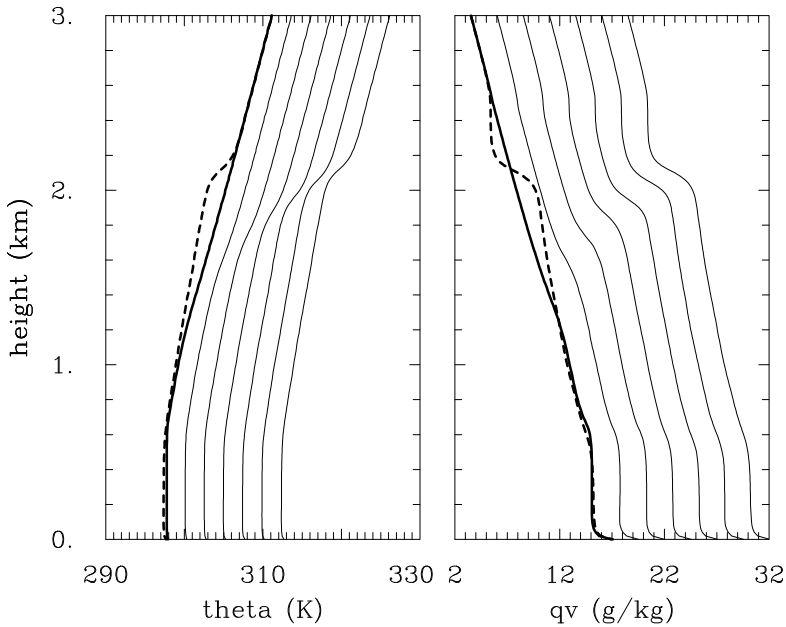


Fig. 1. Evolution of the potential temperature and water vapor mixing ratio profiles in simulation 1000.HM. The thick lines show profiles at 3 hrs (solid line) and 21 hrs (dashed line). Profiles at 6, 9, 12, 15, 18, and 21 hrs (the latter repeated for comparison) are plotted by thin lines, with each profile shifted to the right by 2.5 K for the temperature and 2.5 g kg^{-1} for the water vapor from the corresponding profile at a previous time level. Note that the scale on the horizontal axis applies only to the profiles plotted with thick lines.

subsequent analysis). These changes are accompanied by a gradual increase of convective available potential energy (CAPE) as documented below.

Figure 2 shows the evolutions of the temperature and water vapor inversion heights. The inversion height is defined as the height of the maximum temperature gradient (minimum water vapor gradient) in the mean profile away from the surface. Since the maximum (minimum for the water vapor) is not very pronounced in the first few simulation hours, only data after 5 hr are shown. As Figure 2 shows, the inversion height increases in all simulations at a similar rate. This is true up to about hour 18, where the low-aerosol cases 100.HM and 100.EI begin to show slower increase of the inversion height than high-aerosol cases 1000.HM and 1000.EI. The slower deepening of significantly precipitating shallow convective layers was suggested in Stevens and Seifert (2008) and vanZanten *et al.* (2011), and current results seem consistent with such a suggestion. Prior to hour 18, the rate of change of the inversion height in all simulations is about half a meter per minute, or about 1 cm s^{-1} .

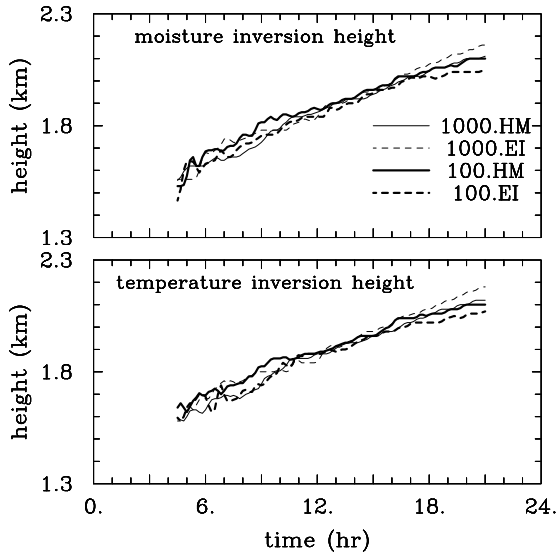


Fig. 2. Evolution of the temperature and moisture inversion heights in four simulations. The inversions are poorly defined *prior* to hour 5 and the data from initial 4 hours are excluded.

3.2 CAPE and surface rainfall

Figure 3 shows the evolutions of CAPE for all simulations. CAPE is calculated as the vertical integral of the positive buoyancy as described in Section 5 of Grabowski *et al.* (1998) except that the condensate loading is included in the calculation (*i.e.*, assuming an adiabatic and not pseudo-adiabatic parcel). The initial conditions for the adiabatic parcel come from the average temperature and moisture within 100-m-deep layer near the surface. As Figure 3 shows, CAPE of the initial sounding is about 30 J kg^{-1} . The initial burst of convection (as in other simulations, see Fig. 3 in vanZanten *et al.* 2011) reduces CAPE to almost zero. After a relatively rapid recovery between hour 1 and 3, CAPE increases in a similar rate in all four simulations until hour 18. After that time, CAPE in low-aerosol simulation 100.EI begins to increase at a significantly higher rate. The other low-aerosol simulation 100.HM starts to show higher rate of CAPE increase around hour 20, and the higher rates in the two pristine simulations are similar. CAPE in high-aerosol simulations keeps increasing at the previous rate. Note that higher CAPE in low-aerosol simulations in final hours coincides with lower inversions (*cf.* Fig. 2) and thus must come from subtle changes of the stratification within the cloud layer. Arguably, higher CAPE in precipitating low-aerosol simulations might be considered surprising because presence of convective precipitation is accompanied by precipitation-

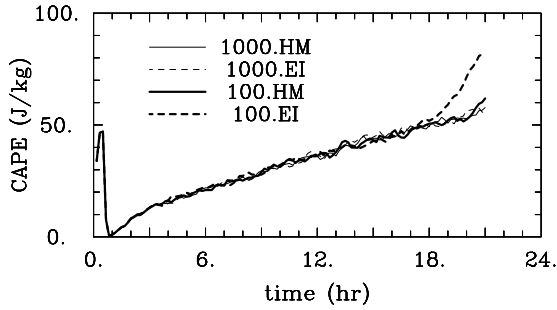


Fig. 3. Evolution of CAPE in four simulations.

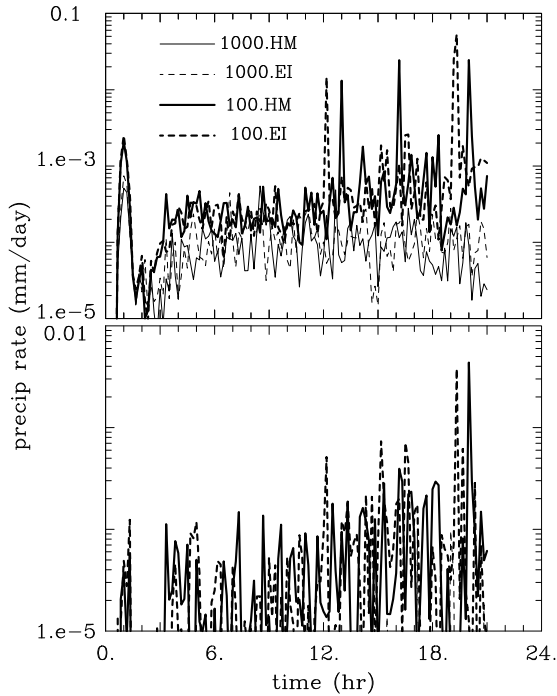


Fig. 4. Evolution of the cloud-base (upper panel) and surface (lower panel) rain rate in four simulations.

laden downdrafts which supply boundary layer with dry and cold low-moist-static-energy air and thus are typically thought to reduce CAPE.

Figure 4 shows the evolution of the domain-averaged rain rate at the height of the cloud base and at the surface. The cloud base height is assumed at 600 m during first three hours of the simulation and linearly decreasing to 500 m at $t = 24$ hr (such a choice comes from the analysis presented later in the paper, *cf.*

Figs. 7-10). As the figure shows, the cloud-base rain rate is significantly higher than at the surface, and – as one might anticipate – it is higher in pristine cases. The rates are nevertheless rather small, approaching domain-averaged surface rates of 0.01 mm day^{-1} in pristine cases toward the end the analyzed period. The largest precipitation rates are arguably associated with the deepest pristine clouds that occasionally occur in the computational domain. Evaporation of rain between the cloud base and the surface leads to the situation where virtually no rain reaches the surface in the polluted case. Overall, the statistics of the precipitation field are strongly affected by the smaller computational domain when compared to vanZanten *et al.* (2011).

3.3 Bulk measures of the cloud field depth

The increase of the inversion height documented in Fig. 2 and gradual increase of CAPE suggests that the averaged depth of the cloud field increases as well. A convenient bulk measure of the evolution of the cloud field depth is the height of the center of mass of various cloud-related fields. Such a measure was first used in simulations of the daytime evolution of convective processes over land, the transition from shallow to deep convection in particular (Grabowski *et al.* 2006). It was subsequently used in Koren *et al.* (2009)¹⁾. Here, we apply this measure to three fields: the cloud mask, the cloud water mixing ratio and the cloud-layer rain mixing ratio. The 3D cloud mask field is locally defined as 1 if $q_c \neq 0$ and 0 otherwise. The cloud-layer rain water mixing ratio is the rain mixing ratio q_r above the cloud base and zero below it (the cloud base is simply assumed at 600 m in this analysis). The height h^q of the center of mass of the field q is defined as

$$h^q = \frac{\int_V z q \, dV}{\int_V q \, dV} = \frac{\int_z z \langle q \rangle \, dz}{\int_z \langle q \rangle \, dz},$$

where the integrals in the middle term are over the entire volume of the computational domain; they are over the vertical extent of the domain in the last term; and $\langle q \rangle (z)$ is the horizontal average of the field q at the height z . For the cloud mask, the $\langle q \rangle (z)$ is simply the cloud fraction profile, whereas the mean profiles of q_c and q_r (the latter truncated to zero below the cloud base) are used to derive the center of mass of the cloud water and cloud-layer rain water.

Figure 5 shows evolutions of the above-defined center-of-mass heights in simulations 100.HM and 1000.HM. There is a striking similarity between the two simulations despite significant differences in the surface precipitation documented in Fig. 4. In both simulations, the cloud-mask center of mass is the

¹⁾Note that Koren *et al.* incorrectly referred to this measure as the center of gravity.

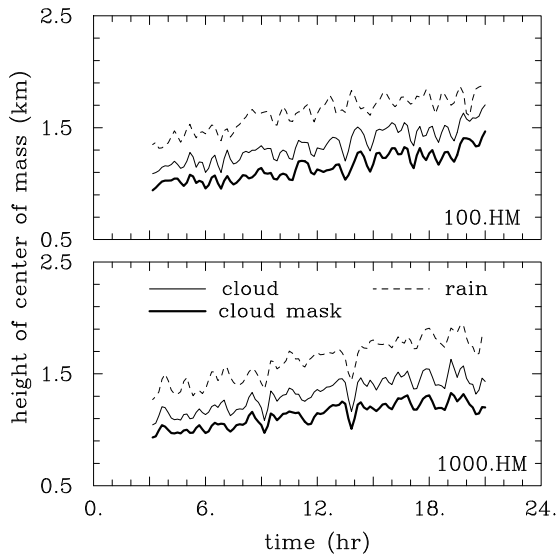


Fig. 5. Evolution of the height of the center of mass of the cloud mask (thick solid line), cloud water field (thin solid line), and cloud-layer rain water field (thin dashed line) in simulations 100.HM and 1000.HM. Original data were filtered with the 1-2-1 filter to smooth temporal variations.

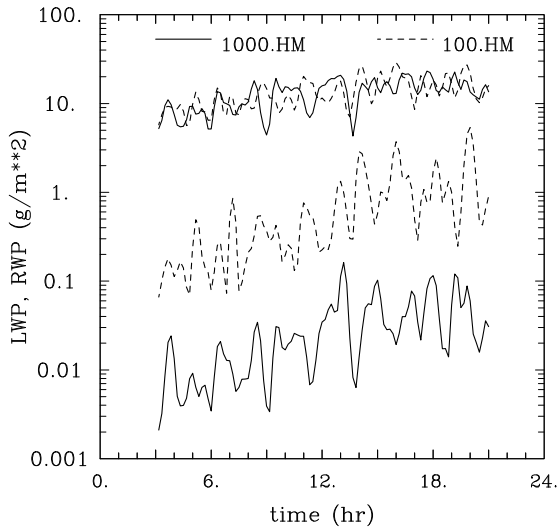


Fig. 6. Evolution of the domain-averaged LWP (upper two curves) and RWP (lower two curves) in simulations 100.HM and 1000.HM. Original data were filtered with the 1-2-1 filter to smooth temporal variations.

lowest. The q_c center of mass is typically about 100 m higher because the cloud water field is top-heavy, that is, the mean cloud water increases with height. The cloud-layer- q_r center of mass is 100 to 150 m above the q_c center of mass. This implies that rain is on average found in upper parts of the cloud field. Rain does fall to the surface (see, for instance, an illustration in Fig. 6 of Stevens and Seifert 2008), but on average it is present mostly in the upper parts of the cloud where the highest cloud water can be found (this also explains why there is little correlation between the cloud-base rain rate and the rain water path). In other words, cloud-layer- q_r is on average even more top-heavy than the cloud water field. As expected, the evolutions of heights of the three fields are highly correlated.

The height of the center of mass of the cloud mask allows estimation of the mean cloud depth. Assuming that clouds have cloud bases at the same height and only differ in their depth, the mean cloud top height is simply twice the difference between the height of the cloud mask center of mass and the cloud base height. This gives the mean cloud top height of around 0.8 km at 6 hrs and around 1.4 km at 21 hrs. Note that these values are significantly smaller than the heights of the inversion, which is between 1.6 and 1.7 km at 6 hrs and between 2.1 and 2.2 km at 21 hrs, depending on the simulation. The cloud depth appears to grow approximately linearly with time, consistent with the changes of the inversion height as documented in Fig. 2.

The analysis of the height of the center of mass provides no information about the mass of cloud and precipitation water within the domain. This is where the difference between low- and high-aerosol simulations shows up as illustrated in Fig. 6. The figure presents the domain-averaged liquid water path (LWP) and rain water path (RWP) for simulations 100.HM and 1000.HM. As the figure shows, the LWP are similar in the two simulations, whereas the RWP differ drastically, with RWP for low-aerosol 100.HM simulation about an order of magnitude higher than in high-aerosol 1000.HM. The increase in time of both LWP and RWP is qualitatively similar to those shown in vanZanten *et al.* (2011; Fig. 3 therein), from single-digit values to over 20 g m^{-2} for LWP, and from around 0.1 to over 5 g m^{-2} for pristine aerosol RWP. The fact that rain water is typically found in the upper parts of the cloud field (*cf.* Fig. 5) explains why there is little correlation between either cloud-base or surface rain rate (Fig. 4) and RWP. The figure for the extremely inhomogeneous mixing simulations shows similar picture.

3.4 Mean cloud droplet concentration

Figure 7 illustrates the evolution of the mean cloud droplet concentration profiles for simulations 100.HM and 1000.HM. The profiles are derived as conditional averages over points with cloud water mixing ratio higher than 0.01 g kg^{-1} . It follows that the profiles also illustrate the increase of the depth

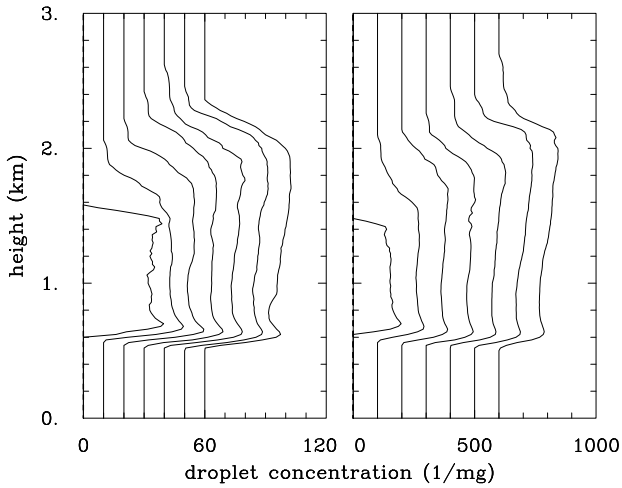


Fig. 7. Evolution of the mean cloud droplet concentration profiles for simulation 100.HM (left panel) and 1000.HM (right panel). The left-most profiles in each panel are instantaneous profiles at 3 hrs and the scales on horizontal axes apply only to them. Profiles at 6, 9, 12, 15, 18, and 21 hrs are averages over past 3 hrs (from data every 10 min) and are shifted to the right by 10 (100) mg^{-1} for 100.HM (1000.HM) from the corresponding profile at a previous time level. Note that the profiles below and above the cloud layer represent the zero line.

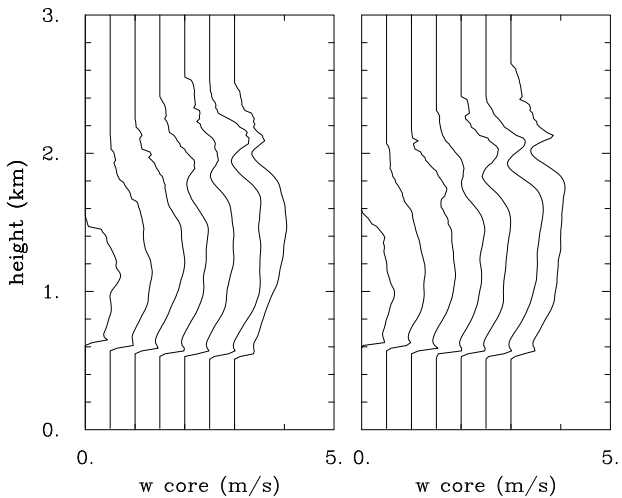


Fig. 8. As Figure 7, but for the mean vertical velocity inside cloud cores. The profiles for hours 6 to 21 are shifted to the right by 0.5 m s^{-1} from the corresponding profile at a previous time level.

of the tallest clouds as the simulations progress. Note that in contrast to the mean cloud depth, the tallest clouds typically reach the height of a couple hundred meters above the inversion. Mean cloud droplet concentrations are typically between 30 and 40 mg^{-1} at 3 hrs for the low-aerosol case 100.HM and between 150 and 200 mg^{-1} for the high-aerosol 1000.HM. As the cloud field deepens, slightly higher droplet concentrations are found in the upper halves of the cloud field in both simulations. Droplet concentration profiles from simulations with extremely-inhomogeneous mixing are similar to those in Fig. 7 and are not shown. The difference in the droplet concentration is responsible for the contrast in the precipitation rates in low- and high-aerosol simulations.

The approximately constant-in-height mean cloud droplet concentration documented in Fig. 7 occurs despite a significant dilution due to entrainment and agrees with RICO observations reported in Gerber *et al.* (2008) and Arabas *et al.* (2009). As discussed in Slawinska *et al.* (2011), the only possible explanation is that a significant in-cloud activation (*e.g.*, activation above the cloud base) takes place in simulated clouds. The in-cloud activation happens across the cloud field depth at the edges of the cloud cores where the updraft is relatively strong and the droplet concentration (and thus the concentration of activated CCN) is reduced due to entrainment. The in-cloud activation here mimics the entrainment-related activation seen in high-resolution single-cloud simulations with bin microphysics discussed in Brenguier and Grabowski (1993), see Slawinska *et al.* (2011) for an extensive discussion.

The relatively low droplet concentrations in current simulations considering the 100 and 1000 mg^{-1} CCN concentrations (*i.e.*, implying activation of only 40% of CCN in the pristine case and less than 25% of CCN in the polluted case) may be considered surprising. However, this is not unrealistic considering the rather low updraft velocities in the cores of simulated clouds as documented in Fig. 8. As the figure shows, the core updraft velocity near cloud base is typically around 0.5 m s^{-1} in both low- and high-aerosol simulations. The core updraft velocity increases with height (which may play some role in in-cloud activation) to reach values close to 1 m s^{-1} in the upper part of the cloud field, especially during second halves of the simulations. The increase is consistent with the increase of CAPE documented in Fig. 3, but overall the velocities seem smaller than those reported in other model simulation by vanZanten *et al.* (2011, *cf.* Fig. 5 therein). The impact of the inversion on the in-cloud vertical velocity field is also apparent in the velocity profiles.

3.5 Cloud fraction and mean cloud width

Figures 9 and 10 present evolutions of the profiles of the cloud fraction and the mean cloud width, respectively. The mean cloud width is derived using a

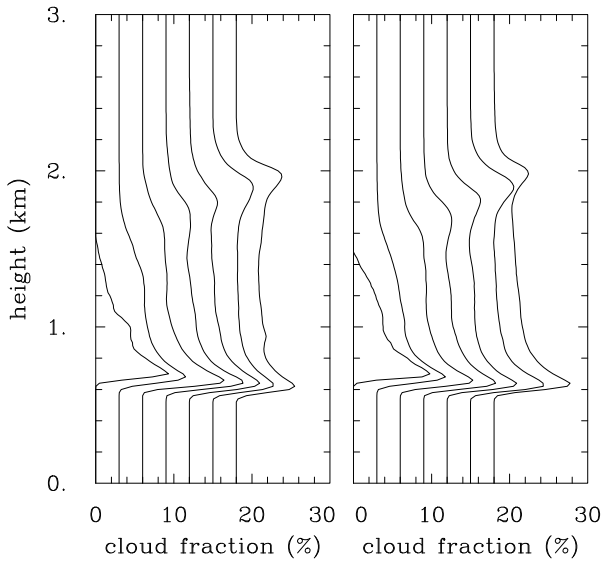


Fig. 9. As Figure 7, but for the mean profiles of the cloud fraction. The profiles for hours 6 to 21 are shifted to the right by 3% from the corresponding profile at a previous time level.

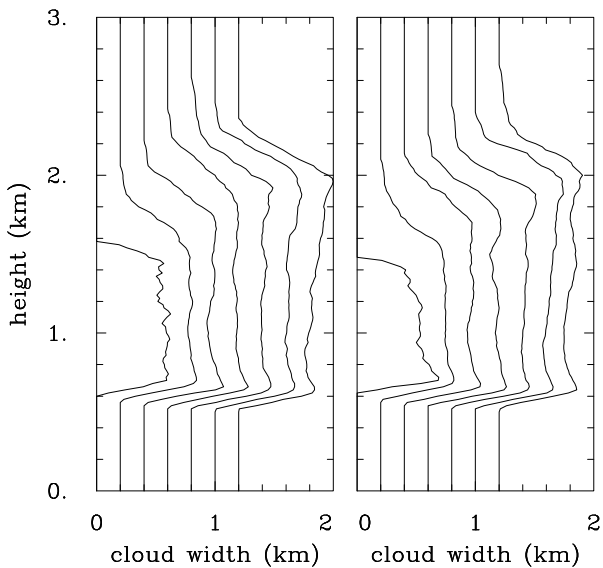


Fig. 10. As Figure 7, but for the mean profiles of the cloud width. The profiles for hours 6 to 21 are shifted to the right by 200 m from the corresponding profile at a previous time level.

simple algorithm detailed in the Appendix. The cloud fraction profiles evolve from those typical for shallow convection under a weak trade-wind inversion to those characteristic for strong-inversion situations. In the former case, the cloud fraction rapidly decreases with height from the maximum near the cloud base (*cf.* Fig. 6 in Siebesma *et al.* 2003). For strong inversions, cloud fraction is more uniform in height and features two maxima, one at the cloud base and another one near the inversion (*cf.* Fig. 7 in Stevens *et al.* 2001). The profiles for low- and high-aerosol simulations evolve in a similar manner. The same is true for the profiles of the mean cloud width shown in Fig. 10. The mean cloud width is around 300 m and appears quite uniform in height. The height at which the mean cloud fraction begins to rapidly decrease is approximately equal to the height of the bottom of the inversion layer (*e.g.*, 1.8 km for hour 12 and 2.0 km for hour 21).

4. DISCUSSION AND CONCLUSIONS

Following the study of non-precipitating shallow convection reported in Slawinska *et al.* (2011), a precipitating case is considered here following the model intercomparison case developed based on RICO observations. The simulations reported here extend EULAG model results contributed to the intercomparison case of vanZanten *et al.* (2011) by applying a sophisticated double-moment warm-rain microphysics of Morrison and Grabowski (2007, 2008). Besides prediction of the cloud droplet and drizzle/rain drop concentrations as in other bulk double-moment schemes, the Morrison and Grabowski scheme predicts the in-cloud supersaturation field and allows secondary activation of cloud droplets above the cloud base. As discussed in Slawinska *et al.* (2011), this feature has a fundamental effect on model results. Yet another important feature of the scheme is a possibility of specifying the homogeneity of the subgrid-scale parameterized turbulent mixing. In a nutshell, one can vary the change of the droplet concentration that accompanies the evaporation of the cloud droplet mixing ratio, from no change at all in the homogeneous mixing case to the extremely inhomogeneous mixing limit where the evaporation does not change the mean volume radius of cloud droplets. Four simulations were performed assuming either pristine or polluted CCN characteristics, each with either homogeneous or extremely inhomogeneous mixing applied uniformly throughout simulated clouds and for the entire simulation.

The simulations featured gradually deepening cloud field and the development of colocated temperature and moisture inversions near the top of the cloud field. The cloud field gradually transitions from what can be referred to as the BOMEX-like shallow convection field as in Siebesma *et al.* (2003) towards the ATEX-like field as in Stevens *et al.* (2001), that is, with the shallow convection layer topped by a strong inversion and the characteristic maximum of the

cloud fraction near the inversion in addition to the maximum near the cloud base. Overall, we find a rather insignificant impact of cloud and precipitation processes on macroscopic characteristics of shallow convection, deepening of the cloud field in particular. Arguably, some of the effects suggested in recent studies briefly reviewed in the introduction can be better exposed by performing either a larger-domain simulations or including an ensemble of simulations, with both approaches providing better statistics of the effects. The main point is, however, that these effects are rather small and they seem to have a rather insignificant impact on model results. It thus follows that including such effects in cloud parameterizations would be difficult.

The above general conclusion needs to be treated with some caution, however. First, simulated clouds still precipitate little and perhaps extending the simulations several hours using larger computational domain would be appropriate to see if precipitation has more significant impact, beyond what is observed in current simulations. An obvious difference between pristine and polluted simulations is the impact on the mean albedo of the cloud field, an aspect documented in Slawinska *et al.* (2011) and not addressed here. One should keep in mind that removing some of the limitations of the modeling setup used here may also lead to additional effects. For instance, applying interactive radiative transfer model in place of prescribed radiative tendencies may enhance differences between clouds developing in pristine and polluted environments through either direct or indirect aerosol impacts. The direct impact comes from different clear-sky radiative cooling profiles associated with different absorbing and scattering properties of pristine and polluted lower-tropospheric aerosols. The indirect effects include impact of contrasting droplet sizes not only on the mean albedo of the cloud field but on cloud absorbing properties as well. We hope to report on such simulations in the future.

Acknowledgements. WWG was partially supported by the NOAA grant NA08OAR4310543, DOE ARM grant DE-FG02-08ER64574, and by the NSF Science and Technology Center for Multi-Scale Modeling of Atmospheric Processes (CMMAP), managed by Colorado State University under cooperative agreement ATM-0425247. JS was supported by the Polish Ministry of Science and Higher Education under grant N N307 126136, by the NOAA grant NA08OAR4310543, and DOE ARM grant DE-FG02-08ER64574. Computer time was provided by NSF MRI Grant CNS-0421498, NSF MRI Grant CNS-0420873, NSF MRI Grant CNS-0420985, NSF sponsorship of the National Center for Atmospheric Research, the University of Colorado, and a grant from the IBM Shared University Research (SUR) program. National Center for Atmospheric Research is sponsored by the National Science Foundation.

APPENDIX

A simple algorithm for the mean cloud width estimation

A simple algorithm to estimate the mean width of a cloud field at a given height assumes that cloud cross sections are close to circular and considers the difference in the area occupied by cloudy gridpoints near cloud edges and those inside. Lets assume that a radius of a single cloud cross section is R and the cloud width is $2R$. In the finite-difference representation of such a cross section, the cloudy cells at the edge of a cloud are assumed to form a ring of the width of approximately the gridlength Δx . In such a case, the area of the part of the cloud cross section that has only cloudy neighbors²⁾ and the area of the entire cloud cross section can be approximated as $\pi(R - \Delta x)^2$ and πR^2 , respectively. The ratio of the two areas is then $s = (R - \Delta x)^2 / R^2$. From the model output, the ratio s can be estimated as the ratio of the number of cloudy points that do not have cloud-free neighbors and the number of all cloudy points (the cloudy/cloud-free gridpoint is defined here as containing more/less than 0.01 g kg^{-1} of cloud water). Once s is known, R can be easily derived as $R = \Delta x / (1 - s^{1/2})$.

The algorithm outlined above is inaccurate for cloudy cross sections occupying just a few gridpoints. For instance, a single cloudy gridpoint or a small ensemble of cloudy gridpoints (say, 1×2 , 2×2 , and 2×3) all contain only points with cloud-free neighbors which implies $s \equiv 0$ and $R = \Delta x$. For a single ensemble of larger sizes, the algorithm returns sensible estimates. For instance, for a single cross section occupying 3×3 , 3×4 , 4×4 , and 5×5 gridpoints, the algorithm gives radius R of $1.5\Delta x$, $1.7\Delta x$, $2\Delta x$, and $2.5\Delta x$, respectively. If there are several clouds in the computational domain, summing up cloud points as described above results in only a slightly different estimate of the mean cloud width than the average of widths for individual cross sections. For instance, for a situations with 2 cloudy cross sections covering 3×3 and 5×5 gridpoints, the average cloud width as given by the mean of the two widths ($1.5\Delta x$ and $2.5\Delta x$) is $2\Delta x$. The algorithm presented above provides a value of $2.1\Delta x$. The algorithm may also work poorly for very-high-resolution cloud simulations (*e.g.*, gridlength in the range of 1 to 10 m) because of complicated spatial structures associated with cloud-environment interfacial instabilities (*cf.* Grabowski and Clark 1991, 1993).

The proposed algorithm is extremely simple because it only requires counting cloudy gridboxes and dividing them between those that have and have not cloud-free neighbors. In contrast, a technique presented in Grabowski *et al.* (2006) (referred to here as the LBA method) requires derivation of the length of cloudy segments along x and y directions, a rather cumbersome procedure.

²⁾The 4 horizontal neighbors of a gridpoint (i, j) are $(i + 1, j)$, $(i - 1, j)$, $(i, j + 1)$, $(i, j - 1)$.

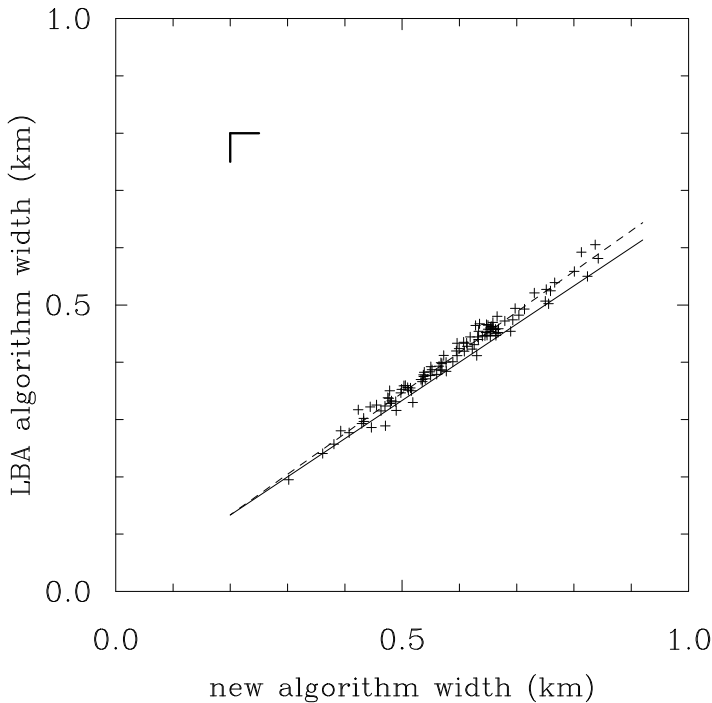


Fig. 11. The mean cloud width derived by the new algorithm *versus* the mean width derived using the LBA method. Data come from the simulation 1000.EI and instantaneous cloud field cross sections at 1-km height saved every 10 min are analyzed for the entire simulation. The dashed line is the least squares fit to the scatterplot. The solid line shows the theoretical relationship with the $2/3$ slope and zero intercept. Short segments in the upper left part depict the model horizontal gridlength.

To illustrate the differences between the two methods, we applied them to one of the simulations described in this paper. The outcome of such an analysis is presented in Fig. 11. The figure shows the scatter-diagram of the widths derived by the two methods for the cloud cross sections at the height of 1 km for the entire length of the simulation. The figure shows that the two methods provide close estimates with the width typically several $\Delta x = 50$ m in length. The LBA method typically gives smaller width because, as pointed out in Grabowski *et al.* (2006), the algorithm based on analysis of cloudy segments results in the underestimation of the circular cloud width. For instance, if a perfectly circular cross section of radius R is intersected along x and y directions, the mean length of cloudy segments is $1.5R$ instead of $2R$, the true cloud width in such a case. This explains why the points on the scatter diagram are aligned close to the line with a slope of 1:1.5.

References

- Albrecht, B.A. (1989), Aerosols, cloud microphysics, and fractional cloudiness, *Science* **245**, 4923, 1227-1230, DOI: 10.1126/science.245.4923.1227.
- Arabas, S., H. Pawlowska, and W.W. Grabowski (2009), Effective radius and droplet spectral width from in-situ aircraft observations in trade-wind cumuli during RICO, *Geophys. Res. Lett.* **36**, L11803, DOI: 10.1029/2009GL038257.
- Bony, S., and J.-L. Dufresne (2005), Marine boundary layer clouds at the heart of tropical cloud feedback uncertainties in climate models, *Geophys. Res. Lett.* **32**, L20806, DOI: 10.1029/2005GL023851.
- Brenguier, J.-L., and W.W. Grabowski (1993), Cumulus entrainment and cloud droplet spectra: A numerical model within a two-dimensional dynamical framework, *J. Atmos. Sci.* **50**, 1, 120-136, DOI: 10.1175/1520-0469(1993)050<0120:CEACDS>2.0.CO;2.
- Chosson, F., J.-L. Brenguier, and M. Schröder (2004), Radiative impact of mixing-processes in boundary layer clouds. **In:** *Proc. 14 Int. Conf. on Clouds and Precipitation, Bologna, Italy*, International Association of Meteorology and Atmospheric Sciences, 371-374.
- Chosson, F., J.-L. Brenguier, and L. Schüller (2007), Entrainment-mixing and radiative transfer simulation in boundary-layer clouds, *J. Atmos. Sci.* **64**, 7, 2670-2682, DOI: 10.1175/JAS3975.1.
- Gerber, H.E., G.M. Frick, J.B. Jensen, and J.G. Hudson (2008), Entrainment, mixing, and microphysics in trade-wind cumulus, *J. Meteor. Soc. Japan* **86A**, 87-106, DOI: 10.2151/jmsj.86A.87.
- Grabowski, W.W. (2006), Indirect impact of atmospheric aerosols in idealized simulations of convective-radiative quasi-equilibrium, *J. Climate* **19**, 18, 4664-4682, DOI: 10.1175/JCLI3857.1.
- Grabowski, W.W., and T.L. Clark (1991), Cloud-environment interface instability: Rising thermal calculations in two spatial dimensions, *J. Atmos. Sci.* **48**, 4, 527-546, DOI: 10.1175/1520-0469(1991)048<0527:CIIRTC>2.0.CO;2.
- Grabowski, W.W., and T.L. Clark (1993), Cloud-environment interface instability, Part II: Extension to three spatial dimensions, *J. Atmos. Sci.* **50**, 4, 555-573, DOI: 10.1175/1520-0469(1993)050<0555:CEIIP1>2.0.CO;2.
- Grabowski, W.W., and P.K. Smolarkiewicz (1990), Monotone finite difference approximations to the advection-condensation problem, *Mon. Weather Rev.* **118**, 10, 2082-2098, DOI: 10.1175/1520-0493(1990)118<2082:MFDATT>2.0.CO;2.
- Grabowski, W.W., and P.K. Smolarkiewicz (1996), Two-time-level semi-Lagrangian modeling of precipitating clouds, *Mon. Weather Rev.* **124**, 3, 487-497, DOI: 10.1175/1520-0493(1996)124<0487:TTLSLM>2.0.CO;2.
- Grabowski, W.W., X. Wu, M.W. Moncrieff, and W.D. Hall (1998), Cloud-resolving modeling of cloud systems during Phase III of GATE. Part II: Effects of resolution and the third spatial dimension, *J. Atmos. Sci.* **55**, 21, 3264-3282, DOI: 10.1175/1520-0469(1998)055<3264:CRMOCS>2.0.CO;2.

- Grabowski, W.W., P. Bechtold, A. Cheng, R. Forbes, C. Halliwell, M. Khairoutdinov, S. Lang, T. Nasuno, J. Petch, W.-K. Tao, R. Wong, X. Wu, and K.-M. Xu (2006), Daytime convective development over land: A model intercomparison based on LBA observations, *Quart. J. Roy. Met. Soc.* **132**, 615, 317-344, DOI: 10.1256/qj.04.147.
- Koren, I., O. Altaratz, G. Feingold, Z. Levin, and T. Reisin (2009), Cloud's Center of Gravity – a compact approach to analyze convective cloud development, *Atmos. Chem. Phys.* **9**, 1, 155-161, DOI: 10.5194/acp-9-155-2009.
- Margolin, L.G., P.K. Smolarkiewicz, and Z. Sorbjan (1999), Large-eddy simulations of convective boundary layers using nonoscillatory differencing, *Physica D* **133**, 1-4, 390-397, DOI: 10.1016/S0167-2789(99)00083-4.
- Morrison, H., and W.W. Grabowski (2007), Comparison of bulk and bin warm-rain microphysics models using a kinematic framework, *J. Atmos. Sci.* **64**, 8, 2839-2861, DOI: 10.1175/JAS3980.
- Morrison, H., and W.W. Grabowski (2008), Modeling supersaturation and subgrid-scale mixing with two-moment bulk warm microphysics, *J. Atmos. Sci.* **65**, 3, 792-812, DOI: 10.1175/2007JAS2374.1.
- Pincus, R., and M.B. Baker (1994), Effect of precipitation on the albedo susceptibility of clouds in the marine boundary layer, *Nature* **372**, 250-252, DOI: 10.1038/372250a0.
- Prusa, J.M., P.K. Smolarkiewicz, and A.A. Wyszogrodzki (2008), EULAG, a computational model for multiscale flows, *Comput. Fluids* **37**, 9, 1193-1207, DOI: 10.1016/j.compfluid.2007.12.001.
- Siebesma, A.P., C.S. Bretherton, A. Brown, A. Chlond, J. Cuxart, P.G. Duynkerke, H. Jiang, M. Khairoutdinov, D. Lewellen, C.-H. Moeng, E. Sanchez, B. Stevens, and D.E. Stevens (2003), A large eddy simulation intercomparison study of shallow cumulus convection, *J. Atmos. Sci.* **60**, 10, 1201-1219, DOI: 10.1175/1520-0469(2003)60<1201:ALESIS>2.0.CO;2.
- Slawinska, J., W.W. Grabowski, H. Pawlowska, and A.A. Wyszogrodzki (2008), Optical properties of shallow convective clouds diagnosed from a bulk-microphysics large-eddy simulation, *J. Climate* **21**, 7, 1639-1647, DOI: 10.1175/2007JCLI1820.1.
- Slawinska, J., W.W. Grabowski, H. Pawlowska, and H. Morrison (2011), Droplet activation and mixing in large-eddy simulation of a shallow cumulus field, *J. Atmos. Sci.*, DOI: 10.1175/JAS-D-11-054.1
- Smolarkiewicz, P.K., and L.G. Margolin (1997), On forward-in-time differencing for fluids: An Eulerian/semi-Lagrangian nonhydrostatic model for stratified flows, *Atmos. Ocean Sp.* **35**, 1, 127-152.
- Stevens, B. (2007), On the growth of layers of nonprecipitating cumulus convection, *J. Atmos. Sci.* **64**, 8, 2916-2931, DOI: 10.1175/JAS3983.1.
- Stevens, B., and A. Seifert (2008), Understanding macrophysical outcomes of microphysical choices in simulations of shallow cumulus convection, *J. Meteor. Soc. Japan* **86A**, 143-162, DOI: 10.2151/jmsj.86A.143.

- Stevens, B., A.S. Ackerman, B.A. Albrecht, A.R. Brown, A. Chlond, J. Cuxart, P.G. Duynkerke, D.C. Lewellen, M.K. Macvean, R.A.J. Neggers, E. Sanchez, A.P. Siebesma, and D.E. Stevens (2001), Simulations of trade wind cumuli under a strong inversion, *J. Atmos. Sci.* **58**, 14, 1870-1891, DOI: 10.1175/1520-0469(2001)058<1870:SOTWCU>2.0.CO;2.
- Twomey, S. (1974), Pollution and the planetary albedo, *Atmos. Environ.* **8**, 12, 1251-1256, DOI: 10.1016/0004-6981(74)90004-3.
- Twomey, S. (1977), The influence of pollution on the shortwave albedo of clouds, *J. Atmos. Sci.* **34**, 7, 1149-1152, DOI: 10.1175/1520-0469(1977)034<1149:TIOPOT>2.0.CO;2.
- vanZanten, M.C., B. Stevens, L. Nuijens, A.P. Siebesma, A. Ackerman, F. Burnet, A. Cheng, F. Couvreux, H. Jiang, M. Khairoutdinov, Y. Kogan, D.C. Lewellen, D. Mechem, K. Nakamura, A. Noda, B.J. Shipway, J. Slawinska, S. Wang, and A. Wyszogrodzki (2011), Controls on precipitation and cloudiness in simulations of trade-wind cumulus as observed during RICO, *J. Adv. Model. Earth Syst.* **3**, M06001, DOI: 10.1029/2011MS000056.
- Warner, J. (1955), The water content of cumuliform cloud, *Tellus* **7**, 4, 449-457, DOI: 10.1111/j.2153-3490.1955.tb01183.x.
- Warner, J. (1968), A reduction in rainfall associated with smoke from sugar-cane fires – An inadvertent weather modification?, *J. Appl. Meteor.* **7**, 2, 247-251, DOI: 10.1175/1520-0450(1968)007<0247:ARIRAW>2.0.CO;2.
- Xue, H., and G. Feingold (2006), Large-eddy simulations of trade wind cumuli: Investigation of aerosol indirect effects, *J. Atmos. Sci.* **63**, 6, 1605-1622, DOI: 10.1175/JAS3706.1.
- Zhao, M., and P.H. Austin (2005a), Life cycle of numerically simulated shallow cumulus clouds. Part I: Transport, *J. Atmos. Sci.* **62**, 5, 1269-1290, DOI: 10.1175/JAS3414.1.
- Zhao, M., and P.H. Austin (2005b), Life cycle of numerically simulated shallow cumulus clouds. Part II: Mixing dynamics, *J. Atmos. Sci.* **62**, 5, 1291-1310, DOI: 10.1175/JAS3415.1.

Received 15 February 2011

Received in revised form 20 June 2011

Accepted 29 June 2011